Turbulent Flow Predictions for Afterbody/Nozzle Geometries Including Base Effects

A. J. Peace*
Aircraft Research Association Ltd., Bedford, England, United Kingdom

A numerical method for solving the Reynolds-averaged Navier-Stokes equations around axisymmetric afterbody/nozzle configurations, with sharp trailing edges or finite bases, is presented. Turbulence closure is achieved through either a simple algebraic turbulence model or a low Reynolds number form of the k-ϵ two-equation differential model. The solution procedure uses an explicit time-marching finite-volume method. The performance of each of the turbulence models is assessed through comparisons with experimental data on three series of geometries, including both attached and separated flow cases.

Nomenclature

a_1 = turbulence structural parameter, = 0.3
C_p = pressure coefficient
$C_{D,p}$ = afterbody pressure drag coefficient
$c_\eta, c_{\epsilon 1} c_{\epsilon 2}, \sigma_k, \sigma_\epsilon$ = constants in k-ϵ model
$d_{\max}$ = afterbody maximum diameter
E = total energy per unit mass
$\boldsymbol{F}, \boldsymbol{G}, \boldsymbol{H}$ = flux vectors
$f_\mu, f_\epsilon, f_{\epsilon 2}$ = wall damping functions in k-ϵ model
H = total enthalpy per unit mass
$\boldsymbol{i}, \boldsymbol{j}$ = unit vectors in (z,r) directions
JPR = P_{o_j}/p_∞
k = turbulent kinetic energy
M = Mach number
$\boldsymbol{n}$ = unit normal vector
n = distance from wall
P_k = production of k
P_o, p = total and static pressure, respectively
Pr, Pr_t = laminar and turbulent Prandtl number, respectively
$\boldsymbol{Q}$ = flux tensor
q_z, q_r = components of heat flux vector
T_o, T = total and static temperature, respectively
t = time variable
u, v = velocity components in (z,r) directions
w = vector of conserved variables
y^+ = boundary-layer scaled coordinate
z, r = axial and radial directions, respectively
z' = axial distance from trailing edge
γ = ratio of specific heats, = 1.4
ϵ = dissipation rate of k
μ, μ_t = laminar and turbulent viscosities, respectively
μ_k, μ_ϵ = effective viscosities in k-ϵ model
ρ = density
$\sigma_{zz}, \sigma_{zr}, \sigma_{rr}, \sigma_{\theta\theta}$ = elements of stress tensor

Subscripts
j = nozzle or jet value
∞ = freestream value

Introduction

THE design of the afterbody and nozzle is critical to the overall performance of both civil and military modern-day aircraft. Traditionally, this design has relied heavily on experimental testing and semiempirical methods. Because a significant part of total aircraft drag (up to 30%) can arise from these components, an accurate theoretical tool could have a clear role as an additional input into the design procedure.

The physics of the flowfield surrounding an afterbody/nozzle geometry is extremely complex, see Fig. 1. A high-pressure jet issues from the nozzle, interacts with the external flow through an inviscid pluming effect and a highly turbulent mixing process, and causes an upstream influence on the afterbody surface pressure field. At certain conditions, the nozzle boundary layer can separate, resulting in a loss of thrust. More frequently, the much thicker afterbody surface boundary layer separates, either as a result of a shock wave interaction or an adverse pressure gradient effect on the steep boattail, resulting in a severe drag penalty. Further, a finite afterbody base implies a recirculating flow region. A useful theoretical method must be able to model all these phenomena. This is proving to be a challenging task for advanced computational techniques.

As with all fluid-dynamic models, there is a trade-off between representing the physical complexity of the flow and computational efficiency. In the application to afterbody/nozzle flowfields, this question has led to two main modeling approaches. The first approach is one in which the flowfield is subdivided into separate regions, each of which is modeled by a different equation set. These regions are then patched together to form a global description of the flowfield. Such methods are efficient, but can lack physical generality. The second type of approach is one in which the Reynolds-averaged Navier-Stokes equations are addressed and the complete flowfield is solved for simultaneously. Efficiency is compromised in this approach for the sake of enhanced physical modeling.

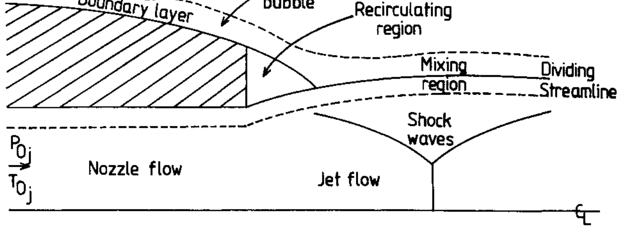

Fig. 1 Schematic of afterbody/nozzle flowfield.

Presented as Paper 89-1865 at the 20th Fluid Dynamics, Plasmadynamics and Lasers Conference, Buffalo, NY, June 12–14, 1989; received July 7, 1989; revision received March 13, 1990.

*Senior Project Supervisor, Aerodynamics Department.

A survey of 18 afterbody prediction methods of both approaches was recently undertaken.[1] It was concluded that no one method was consistently better than the others and that work was needed on Navier-Stokes methods before they could provide viable design tools. A further survey[2] on the ability of Navier-Stokes methods to predict missile base flows also found that the accuracy of certain features, such as base pressure, was not acceptable and that deficiencies in grid resolution and turbulence modeling were likely sources of error.

This paper describes the application of a Navier-Stokes method to axisymmetric afterbody/nozzle configurations. The work described corresponds to the second phase of a body of research aimed at developing methods for such flowfields. Previously, a method based on the viscous/inviscid interaction approach has been developed and reported.[3] Although this method performed reasonably well in certain flow situations, it was obvious that a more general model would be needed if all the physical phenomena present in the flowfield were to be modeled accurately.

The associated turbulence model is critical to the accuracy of Navier-Stokes methods and, to this end, two models are used in the present work. The first is the simple, but computationally efficient, algebraic model due to Baldwin and Lomax,[4] which has been used extensively in this and other applications. The second is a low Reynolds number form of the k-ϵ differential model developed by Chien,[5] which is computationally more expensive but, in principle, should be valid for a wider class of flows than the algebraic model. A primary objective here is to compare these two models.

The Navier-Stokes algorithm used in the present study is a direct extension of the Jameson et al.[6] time-marching finite-volume method for the Euler equations. The thin shear-layer approximation is invoked, whereby diffusion processes in the direction tangential to the afterbody and nozzle surfaces are neglected. The algorithm is described in the main body of the paper, including remarks related to ensuring that artificial dissipation does not swamp the real viscous effects. This is a crucial aspect for all Navier-Stokes methods. Certain stability problems were encountered in the use of both turbulence models, and comments are also made concerning the remedies employed to enhance the robustness of the method.

With reference to the previous remarks on the importance of grid resolution in obtaining accurate predictions for the flows considered here, a feature of the present algorithm is the automatic adaptation of the grid to the flow direction in the wake region. This procedure is also discussed.

To evaluate the performance of the method, predictions are obtained on three series of afterbodies and a comparison is made with experimental data. The first two series have very small base thicknesses and are treated as having sharp trailing edges by the method. Both attached and separated flow cases are examined with each turbulence model. The accuracy of the modeling of the mixing layer is also highlighted. The third series of configurations have large base areas, and emphasis is laid on the quality of base pressure predictions, again for both attached and separated flow on the afterbody.

Numerical Method

The time-dependent axisymmetric Reynolds-averaged Navier-Stokes equations can be written in integral form as

$$\frac{\partial}{\partial t}\int_V w \, \mathrm{d}V + \int_S Q \cdot n \, \mathrm{d}S + \int_V H \, \mathrm{d}V = 0 \qquad (1)$$

where $w = r(\rho, \rho u, \rho v, \rho E)^T$, $Q = F \cdot i + G \cdot j$, H is a source term, and the surface S surrounds the volume V. The vectors F, G, and H are given by

$$F = r(\rho u, \rho u^2 + p - \sigma_{zz}, \rho uv - \sigma_{zr}, \rho uH - u\sigma_{zz} - v\sigma_{zr} + q_z)^T$$

$$G = r(\rho v, \rho uv - \sigma_{zr}, \rho v^2 + p - \sigma_{rr}, \rho vH - u\sigma_{zr} - v\sigma_{rr} + q_r)^T$$

$$H = (0, 0, -p + \sigma_{\theta\theta}, 0)^T$$

where

$$\sigma_{zz} = (\mu + \mu_t)\left[\frac{4}{3}\frac{\partial u}{\partial z} - \frac{2}{3}\left(\frac{\partial v}{\partial r} + \frac{v}{r}\right)\right]$$

$$\sigma_{zr} = (\mu + \mu_t)\left(\frac{\partial u}{\partial r} + \frac{\partial v}{\partial z}\right)$$

$$\sigma_{rr} = (\mu + \mu_t)\left[\frac{4}{3}\frac{\partial v}{\partial r} - \frac{2}{3}\left(\frac{\partial u}{\partial z} + \frac{v}{r}\right)\right]$$

$$\sigma_{\theta\theta} = (\mu + \mu_t)\left[\frac{4}{3}\frac{v}{r} - \frac{2}{3}\left(\frac{\partial u}{\partial z} + \frac{\partial v}{\partial r}\right)\right]$$

$$q_z = -\gamma\left(\frac{\mu}{Pr} + \frac{\mu_t}{Pr_t}\right)\frac{\partial T}{\partial z}, \qquad q_r = -\gamma\left(\frac{\mu}{Pr} + \frac{\mu_t}{Pr_t}\right)\frac{\partial T}{\partial r}$$

The temperature is obtained from the equation of state

$$p = (\gamma - 1)\rho T$$

and

$$\rho E = \frac{p}{\gamma - 1} + \frac{1}{2}\rho(u^2 + v^2), \qquad H = E + \frac{p}{\rho}$$

The eddy viscosity hypothesis has also been employed, so that the effects of turbulence are accounted for by determining μ_t by an appropriate model. The laminar viscosity is given by Sutherland's law.

Equation (1) is discretized using an extension of the finite-volume time-marching method of Jameson et al.[6] Flow variables are stored at cell centers, and the flux balancing reduces to a contour integral around the perimeter of each cell. This essentially gives a conservative central differencing scheme that is second-order accurate on smoothly varying grids. First derivatives are required at the center of cell sides to evaluate the stress and heat flux terms. As a simplification, the thin shear-layer approximation is invoked, whereby only viscous contributions along the radial family of grid lines (see below) are retained, with the assumption that these are the dominant terms in the stress tensor over the majority of the flowfield. This implies that only the first derivatives across the cell sides that are parallel to the afterbody surface are included, and these are evaluated using simple differences between neighboring cell centers. A similar technique is adopted by Swanson and Turkel.[7] With the current grid construction, this procedure assumes that radial rather than normal stresses are used in the stress tensor, the latter being the terms that should be included more exactly in this approximation. For steep afterbodies, this may introduce some error into the method, but it is, in general, not possible to use exactly body-normal grids throughout, particularly near the trailing edge.

The validity of the thin shear-layer assumption has been discussed by other workers, for example, Deiwert.[8] In particular, for base flows, wall dominated viscous effects on the base wall are not modeled, but turbulence effects in this region are small compared with other flowfield features. Evidence is quoted by Sahu[9] to this effect. However, in certain regions of the flowfield, such as at a separation point and a trailing edge, and within a recirculating flow region, the thin-layer assumption will be less valid. This must be balanced with the fact that if the appropriate streamwise viscous terms were included in the method, the grid resolution required to capture the very small length scales in both coordinate directions would prove somewhat prohibitive from a computational viewpoint.

Artificial dissipation is added to Eq. (1) to enable the clean capturing of shock waves and to eliminate undamped modes. Following Jameson,[6] a combination of second and fourth differences is used, with the second difference being controlled by a pressure sensor. Care must be taken to ensure that these artificial effects are significantly smaller than the real viscous effects, so that the true physics is not compromised. This is accomplished here by switching off the differences in the afterbody normal direction within boundary layers and free shear layers. These differences are then gradually reintroduced at the edges of the viscous layers so that, in the inviscid parts of the flow, the original Euler formulation is recovered. This approach is consistent with the thin shear-layer approximation, in that normal to the viscous layers, only the real diffusion terms are present and only the artificial terms are present in the streamwise direction.

The equations of motion are integrated in time using a fourth-order Runge-Kutta scheme with implicit residual smoothing.[10] Local time stepping is used until a steady state is reached.

For the adiabatic flow considered here, zero normal flow, no slip, and zero normal temperature gradient conditions are applied at the afterbody and nozzle surfaces. In line with the previous discussion, the base wall is treated as an inviscid boundary, with a zero normal flow condition only. For the external flow, a freestream Mach number and an initial boundary-layer profile are required. Details of this profile frequently are not measured in experimental tests, so they must be estimated for each calculation. A procedure is adopted here whereby only an initial boundary-layer momentum thickness and shape factor are required, the dependent flow variables then are derived from empirical relations for a flat plate boundary layer. An uncertainty is obviously introduced if the exact experimental inflow conditions are not reproduced. For the internal flow, similar boundary-layer properties are required, along with a jet pressure ratio (*JPR*) and a total temperature ratio. This latter parameter is equal to unity for all the comparisons shown in this paper. Riemann invariants[10] are employed at the far-field boundary, and the nonreflecting condition due to Rudy and Strikwerda[11] is used at the downstream outflow boundary to force the static pressure to its freestream value.

Turbulence Modeling

Two turbulence models are used in the present study. The first is the two-layer algebraic model due to Baldwin and Lomax,[4] which has been used by a number of other authors for the present application. In common with other workers,[12] numerical problems were encountered with this model due to the discontinuity in μ_t across the trailing edge as the inner layer in the formulation abruptly vanishes. The most successful remedy for this problem has been to adopt the procedure described by Mehta et al.,[13] in which the wake turbulent viscosity coefficient is relaxed exponentially from its trailing-edge distribution to one in which the coefficient is determined purely from the outer-layer formulation. The Baldwin-Lomax model has been used by other researchers to compute base flows but, in general, rather ad hoc procedures are employed to adapt the model to flows of this type. In the present work, this model is used only for sharp trailing-edge geometries. The second turbulence model used here is the low Reynolds number form of the k-ϵ model due to Chien.[5] The turbulence equations can be written in the integral form of Eq. (1) as

$$w = r(\rho k,\ \rho\epsilon)^T$$

$$\boldsymbol{F} = r\left(\rho uk - \mu_k\frac{\partial k}{\partial z},\quad \rho u\epsilon - \mu_\epsilon\frac{\partial \epsilon}{\partial z}\right)^T$$

$$\boldsymbol{G} = r\left(\rho vk - \mu_k\frac{\partial k}{\partial r},\quad \rho v\epsilon - \mu_\epsilon\frac{\partial \epsilon}{\partial_r}\right)^T$$

$$\boldsymbol{H} = -r\left(P_k - \rho\epsilon - \frac{2\mu k}{n^2},\quad c_{\epsilon 1}\frac{\epsilon}{k}P_k - c_{\epsilon 2}f_{\epsilon 2}\rho\frac{\epsilon^2}{k} - \frac{2\mu f_\epsilon \epsilon}{n^2}\right)^T$$

where

$$\mu_t = c_\mu f_\mu \frac{\rho k^2}{\epsilon},\qquad c_\mu = 0.09,\qquad f_\mu = 1 - \exp(-0.0115y^+)$$

$$f_\epsilon = \exp(-0.5y^+),\qquad f_{\epsilon 2} = 1 - 0.222\exp[-(\rho k^2/6\mu\epsilon)^2]$$

$$c_{\epsilon 1} = 1.35,\quad c_{\epsilon 2} = 1.8,\quad \mu_k = \mu + \mu_t/\sigma_k,\quad \mu_\epsilon = \mu + \mu_t/\sigma_\epsilon,$$

$$\sigma_k = 1,\quad \sigma_\epsilon = 1.3$$

The production term is evaluated here as

$$P_k = \mu_t\left(\frac{\partial u}{\partial r} + \frac{\partial v}{\partial z}\right)^2$$

This form of the k-ϵ model enables calculations to proceed down to the wall surface via the use of wall damping terms, which eliminates the need for wall functions and the uncertainty that they imply for separated flow. The diffusion terms in the k and ϵ equations are treated exactly as for the mean flow equations, but the convective terms are treated differently. Instead of averaging neighboring cell centers to obtain a cell-side quantity for the contribution to the convective flux balance, the immediate upstream quantity is used. Thus, a first-order accurate conservative upwind differencing scheme

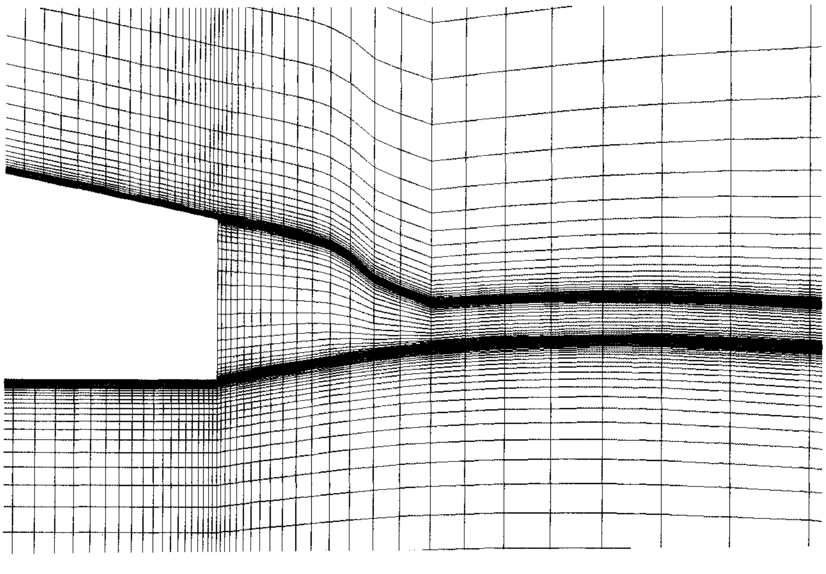

Fig. 2 Grid for geometry with base at solution convergence.

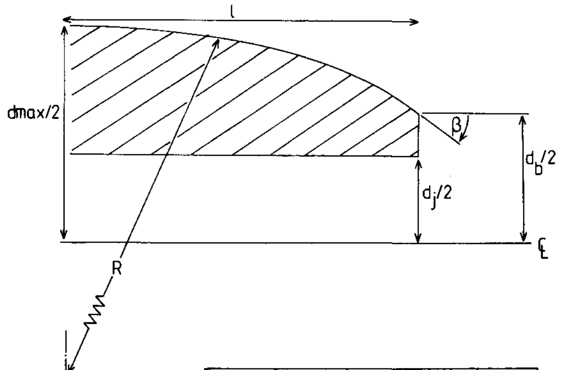

		l/d_{max}	d_b/d_{max}	d_j/d_{max}	R/d_{max}	β.deg	
Model	1B	1·83	0·60	0·40	8·51	12·4	Ref. 26
Model	2B	1·37	0·60	0·40	4·81	16·6	
Model	3B	1·09	0·60	0·40	3·10	20·7	
Model	4B	0·91	0·60	0·40	2·16	24·8	
Config.	1	0·80	0·50	0·50	1·43	34·0	Ref. 19,20
Config.	2	1·00	0·50	0·50	2·16	27·5	
Config.	3	1·77	0·50	0·50	6·50	15·8	

Fig. 3 Circular arc geometries.

is used for the convection of the turbulence variables. This treatment, although being less accurate than the basic scheme, enhances the stability of the method. A similar procedure was adopted by Thomas et al.[14] when they also encountered stability problems in their afterbody method. Because of the inherent dissipative qualities of an upwind differencing scheme, no additional artificial dissipation is added explicitly to the k and ϵ equations.

The mean flow and turbulence equations are marched in time simultaneously. The source terms in the turbulence equations can be destabilizing, and it has been found necessary to evaluate them at the first of the four stages in the Runge-Kutta scheme and then to hold them at constant values through the remainder of the stages.

One of the main difficulties encountered when using the k-ϵ model is ensuring that k and ϵ remain non-negative during the time-stepping procedure. The upwind differencing scheme helps to alleviate this problem, but problems can still occur, particularly very close to body surfaces in the region where the wall damping terms operate. In these regions, unrealistically small values of ϵ can result in large and unstable values of μ_t. A further useful technique employed here is to introduce a lower bound on ϵ, which can be decreased during the time integration so that, when a steady state is reached, its previous influence has vanished..

The boundary conditions for k and ϵ are that they vanish at solid surfaces, are specified at inflow boundaries and are extrapolated at outflow boundaries. Again, the prescription of k and ϵ at inflow from experimental data is usually not possible, and so profiles are generated from a mixing length definition of the turbulent viscosity, the relation

$$\rho k = \mu_t \left| \frac{\partial u}{\partial y} \right| a_1$$

and the definition of μ_t in terms of k and ϵ.

Grid Generation and Adaptation

The grid generation procedure consists of a sequence of simple shearing and stretching transformations to an initial Cartesian grid. For viscous flow solutions, grid spacing must be compressed in the region close to the afterbody and nozzle walls and the wake centerline to capture the details of the shear layers. The height of the first cell on the body surface and the axial spacing at the trailing edge, together with the extent of the outer boundaries, are sufficient to determine the computational grid in the procedure used here. In the medium and far wake regions, it is possible to increase the radial spacing with axial distance from the trailing edge. As the wake relaxes, the radial gradients in flow quantities decrease and the need for a fine grid diminishes. This procedure increases the maximum allowable time step in these regions, which improves the convergence rate.

A number of recent papers on afterbody flows,[15-18] particularly those with base flow representation, have stressed the need to align grid lines with dominant flow features. In the present work, the grid is automatically adapted, during the time integration, so that the trailing-edge grid line is coincident with the trailing-edge streamline. (For a finite base geometry, two such lines will be present.) Flow variables are interpolated after each movement of the grid. For sharp trailing-edge flows, this procedure provides a clustering of grid points at the center of the highly turbulent wake mixing region, whereas for base flows, grid points are concentrated around the recirculation region. In the latter case, it is crucial that grid density is high within the turbulent shear layers, as it is the shear stresses that primarily drive the recirculatory flow and, hence, determine the base pressure. Also, the representation of the Prandtl-Meyer expansion around the nozzle lip is enhanced if the grid follows the flow direction[18] (the expansion angle). Figure 2 shows a close-up of the grid in the vicinity of the base of a typical geometry at the point when a converged solution hs been obtained.

Results and Discussion

The Navier-Stokes algorithm described in the previous sections is now applied to a number of axisymmetric afterbody/nozzle geometries. For a number of the geometries examined in this section, grid sensitivity studies have been performed. The details of these studies are not included here, but all results shown have been obtained on fine grids, and it is considered that they are, in the main, grid independent. The circular arc configurations tested by Reubush and Runckel[19] and Mason and Putnam[20] are addressed first. The geometrical details are given in Fig. 3. These geometries are considered as having sharp trailing edges, in common with their use for many previous method evaluations (see Ref. 1), so that the nozzle radius is slightly increased to close down the trailing edge. Results from both the algebraic and differential turbulence models have been obtained for the modified geometries.

Figure 4 shows the afterbody pressure distributions on the shallowest geometry (configuration 3) at $M_\infty = 0.8$ and $JPR = 2.9$, at which condition the flow remains attached. It can be seen that results from using each turbulence model are similar and compare favorably with the experimental data. The differences between the Navier-Stokes results for this case

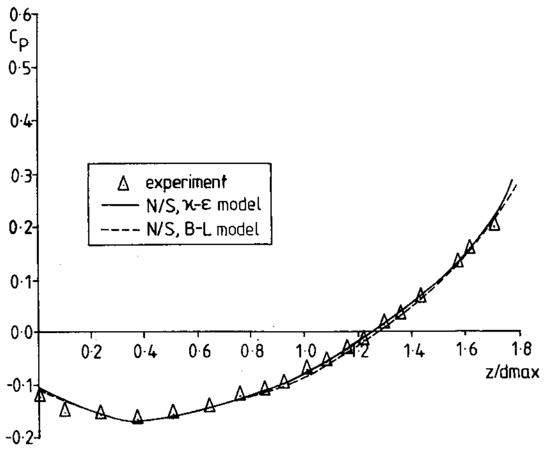

Fig. 4 Configuration 3—$M_\infty = 0.8$, $JPR = 2.9$.

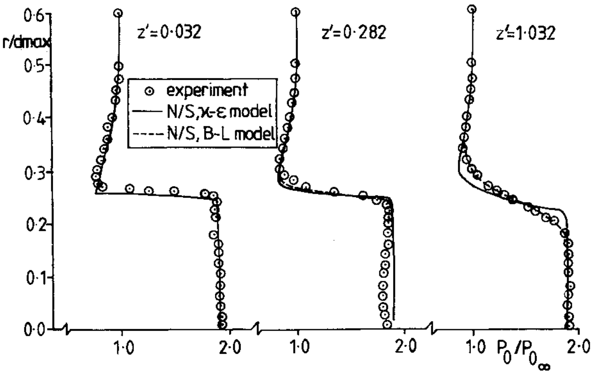

Fig. 5 Configuration 3, mixing layer—$M_\infty = 0.8$, $JPR = 2.9$.

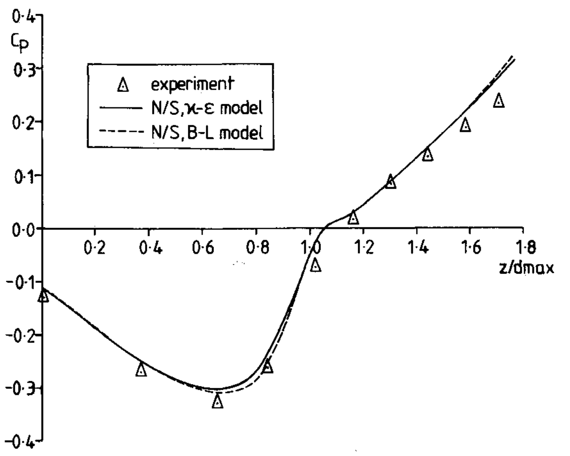

Fig. 6 Configuration 3—$M_\infty = 0.96$, $JPR = 4.09$.

are more amplified in the mixing layer predictions of Fig. 5. Rather surprisingly, the Baldwin-Lomax model gives the better prediction, although, as it was basically developed for boundary-layer flows, one can only assume that this is rather fortuitous. The k-ϵ model might have been expected to give good predictions for the mixing layer development because of its superior level of physical modelling. However, it appears that the model is underestimating the mixing and, hence, the entrainment of fluid from the external flow region. Other previously published comparisons[21,22] have also observed the same trends and, at present, the reason for this discrepancy is unknown. However, Ref. 22 demonstrates that the mixing layer development is strongly dependent on the turbulence properties at the trailing edge. A highly detailed set of experimental data, including turbulent stresses, may help to resolve this issue.

Figure 6 shows a comparison of afterbody pressures on the same geometry, but at $M_\infty = 0.96$ and $JPR = 4.09$. Again, there is little difference between predictions. The shock wave is reasonably modeled, but the trailing-edge pressure is overpredicted. This probably signifies a worsening of the prediction of the near wake mixing layer (experimental data not available) from both turbulence models, with an underestimation of the entrainment seriously affecting the flow development on the rear portion of the afterbody.

It is interesting at this point to examine the afterbody pressure drag predictions as a function of jet pressure ratio for the attached flows on configuration 3. Such plots for two freestream Mach numbers, one giving subcritical and the other supercritical flow on the afterbody surface, are given in Fig. 7. For the lower Mach number, reasonable agreement with experiment is obtained, although the reduction in drag at low jet pressure ratio is not predicted. The entrainment effect dominates the flow at these values, and this is another indication that the method is not picking up the detailed effects of this phenomenon. At the higher Mach number, only the trend with high values of jet pressure ratio is obtained. For both Mach numbers, the k-ϵ model gives the lower drag prediction in all cases. Turning to configuration 1, the steepest afterbody tested, a comparison of afterbody pressures is shown in Fig. 8 at $M_\infty = 0.8$ and $JPR = 2.9$. As can be seen from the experimental data, the external boundary layer separates to give a pressure plateau near the trailing edge. Neither of the turbulence models reproduces this plateau, with the k-ϵ model slightly giving the superior pressure levels. The theoretical separation positions are also marked on the figure. It is well known that algebraic turbulence models give poor predictions for separated flow due to the lack of upstream influence in the turbulence levels. A popular remedy is to append the relaxation method of Shang and Hankey[23] to the Baldwin-Lomax model to attempt to account for these effects. This modification also was used in the present work, but no uniformity in the values of the empirical constants required in the model, to give good predictions for separated flow, was found over a wide range of cases. The differential model obviously has a natural upstream mechanism, via the convection of turbulence quantities, but there would still appear to be a marked deficiency in its ability to model accurately separated flow regions.

Mixing layer predictions for this case are plotted in Fig. 9. The trends observed for the attached flow result discussed earlier are also reproduced here. Neither of the results pre-

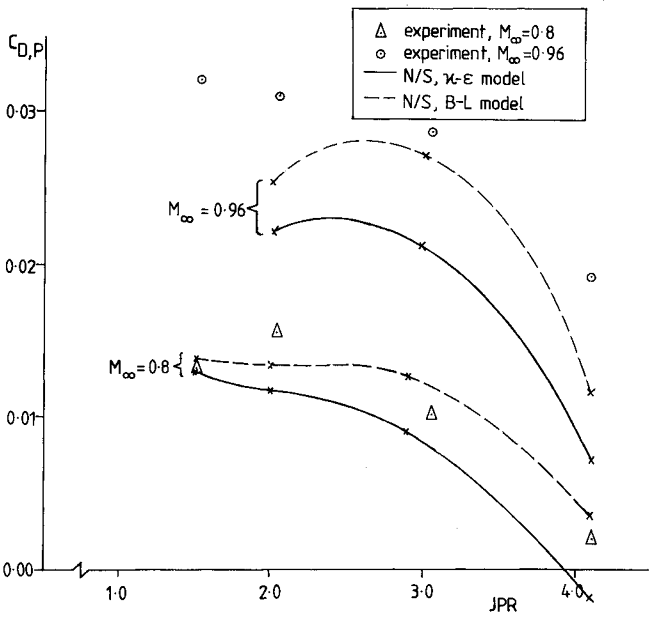

Fig. 7 Configuration 3—pressure drag coefficient.

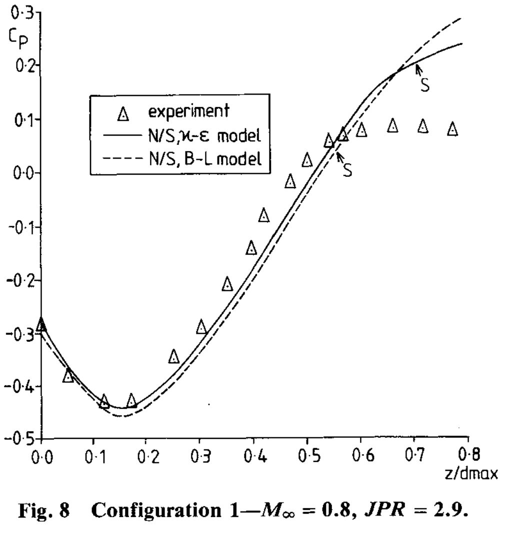

Fig. 8 Configuration 1—$M_\infty = 0.8$, $JPR = 2.9$.

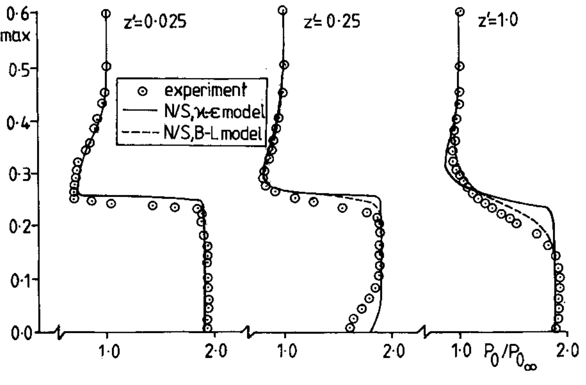

Fig. 9 Configuration 1, mixing layer—M_∞ = 0.8, JPR = 2.9.

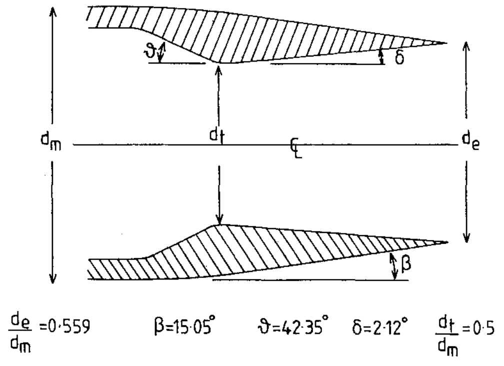

Fig. 10 Configuration 1, Ref. 24 geometry.

dicted adequately the total pressure loss downstream of the Mach disc on the centerline, as can be seen in the profiles at z' = 0.25. It is probable that a much refined computational grid is required in the region of this phenomenon to capture its physical effect on the flowfield.

The next geometry considered is configuration 1 of Ref. 24, the geometrical details of which are given in Fig. 10. The afterbody and nozzle surface pressure distributions at M_∞ = 0.8 and JPR = 3.09 are shown in Figs. 11a and 11b, again for both turbulence models. Agreement on the afterbody is generally favorable for this attached flow case, although, in common with Fig. 6, the predicted trailing-edge pressures are slightly too high. Comparison on the nozzle surface is also favorable, except that the rapid flow expansion approaching the throat is slightly in error. It is believed that a refinement of the computational grid in the axial direction in this region would improve the comparison.

At a higher Mach number, M_∞ = 0.94, the shock boundary-layer interaction on the afterbody is sufficiently severe to cause flow separation. As shown in Fig. 12, the algebraic model again performs poorly in this situation, but the k-ϵ model gives a much improved prediction. The discrepancy between theory and experiment is still marked for the k-ϵ model, but comparison of Fig. 8 with Fig. 12 appears to indicate that the differential model affords a larger improvement over the algebraic model for a shock wave associated separation than for a smooth adverse pressure gradient separation. However, the present evidence is limited in this respect, and it would be desirable to examine a larger number of cases to see if this statement is generally more valid. Aerofoil calculations by

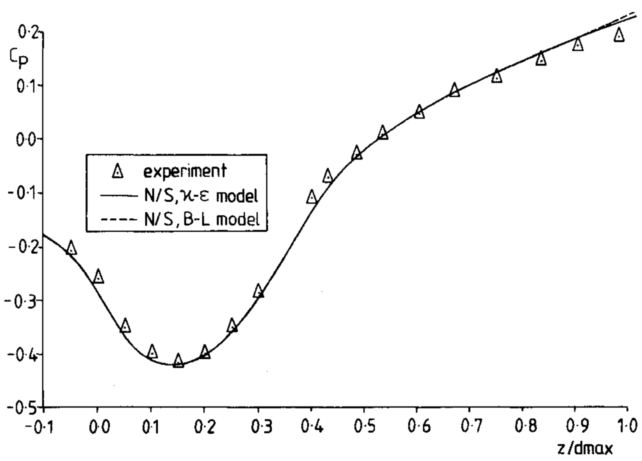

Fig. 11a Geometry as Fig. 10—M_∞ = 0.8, JPR = 3.09, afterbody surface.

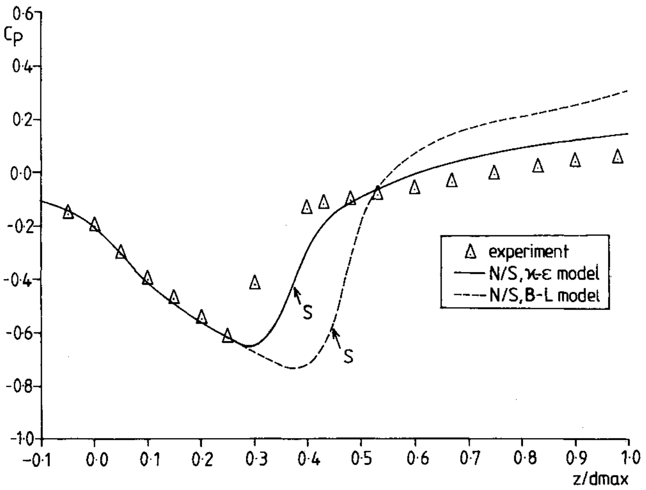

Fig. 12 Geometry as Fig. 10—M_∞ = 0.94, JPR = 3.02, afterbody surface.

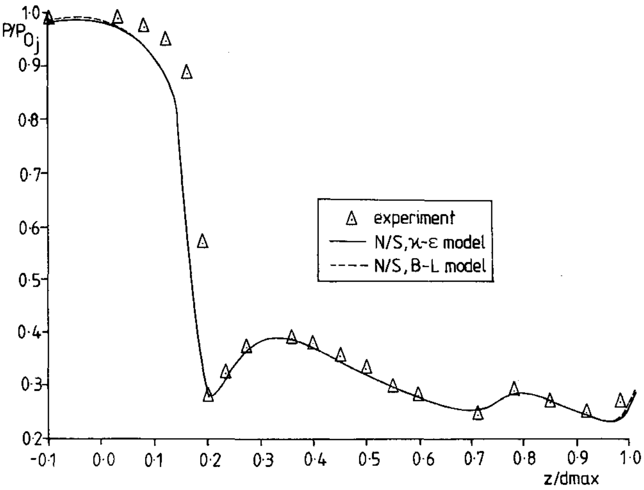

Fig. 11b Geometry as Fig. 10—M_∞ = 0.8, JPR = 3.09, nozzle surface.

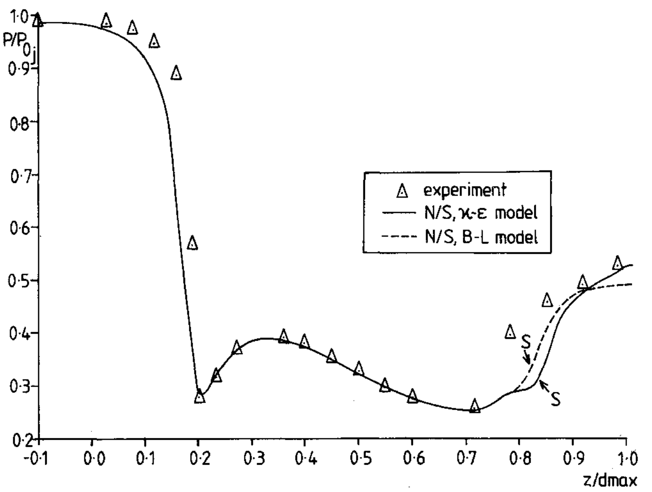

Fig. 13 Geometry as Fig. 10—M_∞ = 0.8, JPR = 2.01, nozzle surface.

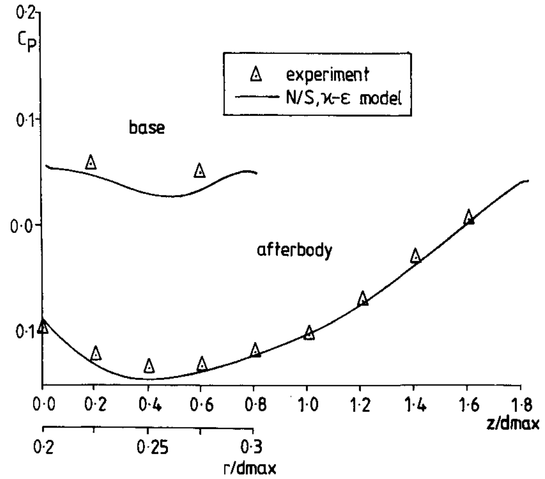

Fig. 14 Model 1B—$M_\infty = 0.8$, $JPR = 3.5$.

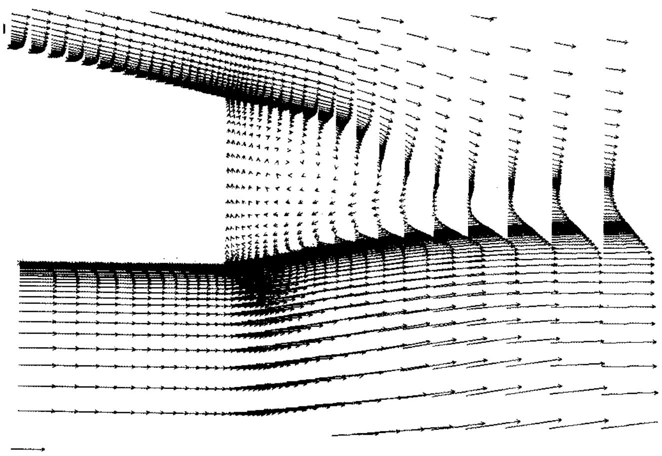

Fig. 15 Model 1B—$M_\infty = 0.8$, $JPR = 3.5$, velocity vectors.

Coakley[25] using the full Navier-Stokes equations show similar discrepancies when using the k-ϵ model to compute shock induced separations, and so it is unlikely that this feature is caused by the thin shear-layer approximation. It may be inferred that the discrepancy in Fig. 8 is also not due to this approximation.

If the jet pressure ratio is sufficiently low, flow separation from the nozzle surface takes place, and an example of this situation is demonstrated in Fig. 13 at $JPR = 2.02$ ($M_\infty = 0.8$). Results from using each turbulence model are similar and both position the rapid compression region too far downstream, presumably due to incorrectly predicting the separation point too close to the trailing edge.

The final geometries considered are the thick base configurations tested by Reid and Kurn,[26] shown in Fig. 3. Only the k-ϵ turbulence model has been used for these geometries. The predicted pressure distribution along the afterbody and base of model 1B at $M_\infty = 0.8$ and $JPR = 3.5$ is compared with experimental data in Fig. 14. The afterbody distribution is reasonably well predicted for this attached flow, although the lack of an experimental data point near the trailing edge makes it rather difficult to give a strong statement about the accuracy of the theoretical results. The pressure along the base is accurate to about 0.01 in C_p at the data point positions. It is difficult to know whether the real flow follows the theory in showing a decrease in pressure toward the center of the base, but physically, a fairly constant pressure across the base may have been expected.

The technique of adapting the grid gives a good definition of the recirculating flow in the base region, as can be seen in the velocity vector plot in Fig. 15. A single rotating bubble is apparent, whose perimeter is well defined due to the enforced grid concentration. The expansion of the flow around the nozzle lip also is clearly brought out in this figure.

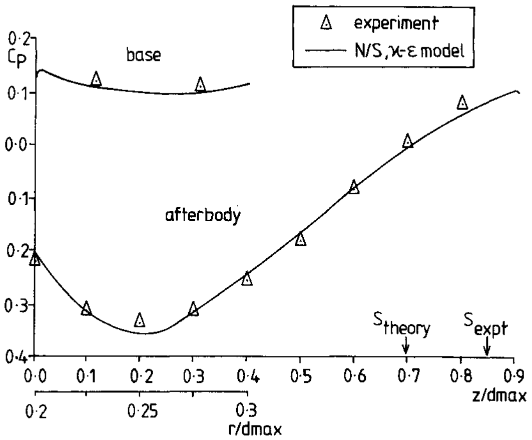

Fig. 16 Model 4B—$M_\infty = 0.8$, $JPR = 3.5$.

Finally, results on model 4B, the steepest afterbody tested, are presented in Fig. 16. The flow separates on the afterbody but, in contrast to the previous separated flow cases discussed in this section, the pressure is under rather than overpredicted. The predicted separation position is further upstream than the experimentally observed position, which is consistent with the previous pressure levels. Whether this differing behavior is due to the presence of the base in the present case is unknown. The base pressure appears to be quite well predicted.

Of the results described in this section, those obtained with the Baldwin-Lomax turbulence model were run at a Courant-Friedricks-Lewy (CFL) = 4.2 and required, on average, 4000 time steps to reduce the average residual (rate of change of density) by four orders of magnitude. This corresponds to a CPU time of 2500 s on a CRAY 1S. Generally, graphical accuracy is obtained in half this time. Results obtained with the k-ϵ turbulence model were run at a CFL = 3.0, using a Baldwin-Lomax solution as initial conditions, for a further 2500 times steps, corresponding to a CPU time of 3000 s. Again a somewhat reduced convergence level would be sufficient for graphical accuracy.

Conclusions

A Navier-Stokes method for calculating axisymmetric afterbody/nozzle flowfields, including base effects, has been presented. Turbulence closure has been achieved with both an algebraic and a two-equation (k-ϵ) differential model. The solution algorithm is of the time-marching finite-volume type, and the thin shear-layer approximation is invoked. Predictions from the method have been compared with experimental data from a number of sources, on circular arc geometries both with and without bases, and on a conical afterbody with a convergent-divergent nozzle. These comparisons show that attached flows are predicted equally well with either turbulence model, but both models are deficient in their prediction of separated flow regions. It is possible that more advanced models are required in this respect. Based on the test cases examined, it also appears that the differential model underestimates the rate of mixing in the wake region and, hence, the entrainment of fluid from the external flow to the jet region, which causes a degradation in the quality of the trailing-edge pressure. Base pressure is reasonably well predicted, at least for the subsonic external flow cases examined here.

Acknowledgment

This work was carried out under contract to the United Kingdom Ministry of Defence (Procurement Executive).

References

[1]Sacher, P. (ed.), "Aerodynamics of Aircraft Afterbody," AGARD AR 226, 1986.

[2]Petrie, H. L., and Walker B. J., "Comparison of Experiment and Computation for a Missile Base Region Flowfield with a Centered Propulsive Jet," AIAA Paper 85-1618, 1985.

[3]Peace, A. J., "A Method for Calculating Axisymmetric Afterbody Flows," *Journal of Propulsion and Power*, Vol. 3, July 1987, pp. 357-364.

[4]Baldwin, B. S., and Lomax, H., "Thin Layer Approximation and Algebraic Model for Turbulent Separated Flows," AIAA Paper 78-257, 1978.

[5]Chien, K. Y., "Predictions of Channel and Boundary Layer Flows with a Low-Reynolds-Number Turbulence Model,"*AIAA Journal*, Vol. 20, Jan. 1982, pp. 33-38.

[6]Jameson, A., Schmidt, W., and Turkel, E., "Numerical Solution of the Euler Equations by Finite Volume Methods Using Runge-Kutta Time-Stepping Schemes," AIAA Paper 81-1259, 1981.

[7]Swanson, R. C., and Turkel, E., "A Multistage Time-Stepping Scheme for the Navier-Stokes Equations," AIAA Paper 85-0035, 1985.

[8]Deiwert, G. S., "A Computational Investigation of Supersonic Axisymmetric Flow over Boattails Containing a Centred Propulsive Jet," *AIAA Journal*, Vol. 22, Oct. 1984, pp. 1358-1365.

[9]Sahu, J., "Three Dimensional Base Flow Calculation for a Projectile at Transonic Velocity," AIAA Paper 86-1051, 1986.

[10]Jameson, A., and Baker, T. J., "Solution of the Euler Equations for Complex Configurations," AIAA Paper 83-1929, 1983.

[11]Rudy, D., and Strikwerda, J., "A Non-Reflecting Outflow Boundary Condition for Subsonic Navier-Stokes Calculations," *Journal of Computational Physics*, Vol. 36, Jan. 1980, pp. 55-70.

[12]Thomas, P. D., "Numerical Method for Predicting Flow Characteristics and Performance of Non-Axisymmetric Nozzles," NASA CR 3264, 1980.

[13]Mehta, U., Chang, K. C., and Cebeci, T., "Relative Advantages of Thin-Layer Navier-Stokes and Interactive Boundary-Layer Procedures," NASA TM 86778, 1985.

[14]Thomas, P. D., Reklis, R. P., Roloff, R. R., and Conti, R. J., "Numerical Simulation of Axisymmetric Base Flow on Tactical Missiles with Propulsive Jet," AIAA Paper 84-1658, 1984.

[15]Venkatapathy, E., Lombard, C. K., Bardina, J., and Luh, R. C.-C., "Accurate Numerical Simulation of Supersonic Jet Exhaust Flow with CSCM on Adaptive Overlapping Grids," AIAA Paper 87-465, 1987.

[16]Hoffman, J. J., Birch, S. F., Hopcroft, R. G., and Holcomb, J. E., "Navier-Stokes Calculations of Rocket Base Flows," AIAA Paper 87-466, 1987.

[17]Childs, R. E., and Caruso, S. C., "On the Accuracy of Turbulent Base Flow Predictions," AIAA Paper 87-1439, 1987.

[18]Caruso, S. C., and Childs, R. E., "Aspects of Grid Topology for Reynolds-Averaged Navier-Stokes Base Flow Computations," AIAA Paper 88-523, 1988.

[19]Reubush, D. E., and Runckel, J., "Effect of Fineness Ratio on Boattail Drag on Circular-Arc Afterbodies Having Closure Ratios of 0.50 with Jet Exhaust at Mach Numbers Up to 1.3," NASA TN D-7192, 1973.

[20]Mason, N. L., and Putnam, L. E., "Pitot Pressure Measurements in Flow Fields Behind Circular-Arc Nozzles with Exhaust Jets at Subsonic Free-Stream Mach Numbers," NASA TM 80169, 1979.

[21]Cline, M. C., and Wilmoth, R. G., "Computation of High Reynolds Number Internal/External Flows," *AIAA Journal*, Vol. 21, Feb. 1983, pp. 172-173.

[22]Wilmoth, R. G., "Viscous/Inviscid Calculations of Jet Entrainment Effects on Subsonic Flow Over Nozzle Afterbodies," NASA TR-1626, 1980.

[23]Shang, J. S., and Hankey, W. L., "Numerical Solution of Supersonic Turbulent Flow Over a Compression Ramp," *AIAA Journal*, Vol. 13, Oct. 1978, pp. 1368-1374.

[24]Carson, G. T., and Lee, E. E., "Experimental and Analytical Investigation of Axisymmetric Supersonic Cruise Nozzle Geometry at Mach Numbers from 0.6 to 1.3," NASA TP 1953, 1981.

[25]Coakley, T. J., "Impact of Turbulence Modelling on Numerical Accuracy and Efficiency of Compressible Flow Simulations," NASA TM 88333, 1988.

[26]Reid, J., and Kurn, A. G., "The Effect of Boundary Layer Thickness on Afterbody Drag," Royal Aircraft Establishment, TR 79083, 1979.